Proceedings of the ASME 2024 19th International Manufacturing Science and Engineering Conference
MSEC2024
June 17-21, 2024, Knoxville, Tennessee

MSEC2024-122414

BRIEF PAPER: GEOMETRIC DETERMINANTS OF MATERIAL JETTING-ENABLED BI-MATERIAL INTERFACE INTEGRITY USING POLYJET 3D PRINTING

Nolan J. Aberdeen
University of Maryland
College Park, MD

Kimia Forghani
University of Maryland
College Park, MD

Ryan D. Sochol
University of Maryland
College Park, MD

ABSTRACT

Among the wide range of additive manufacturing—or "three-dimensional (3D) printing"—technologies, "material jetting" approaches are distinctively suited for multi-material fabrication. Because material jetting strategies, such as "PolyJet 3D printing", harness inkjets that allow for multiple photopolymer droplets (and sacrificial support materials) to be dispensed in parallel to build 3D objects, distinct materials with unique properties can be readily unified in a single print akin to combining multiple-colored inks using a conventional 2D color printer. Although researchers have leveraged this multi-material capability to achieve, for example, 3D functionally graded and bi-material composite systems, there are cases in which the interface between distinct materials can become a key region of mechanical failure if not designed properly. To elucidate potential design factors that contribute to such failure modes, here we investigate the relationship between the interface design and tensile mechanical failure dynamics for PolyJet-printed bi-material coupons. Experimental results for a select set of bi-material sample designs that were 3D printed using a Stratasys Objet500 Connex3 PolyJet 3D printer and subjected to uniaxial tensile testing using a Tinius Olsen H25K-T benchtop universal testing machine under uniaxial strain revealed that increasing the surface contact area between two distinct materials via changes in geometric design does not necessarily increase the interface strength based on the length scales and loading conditions investigated in the current study and that further studies of the role of multi-material geometric designs in interface integrity are warranted to understand potential mechanisms underlying these results. Given the increasing interest in material jetting—and PolyJet 3D printing in particular—as a pathway to multi-material manufacturing in fields including robotics and fluidic circuitry, this study suggests that multi-material interface geometry should be considered appropriately for future applications.

Keywords: PolyJet, Additive Manufacturing, 3D Printing

1. INTRODUCTION

Bi-material and composite systems offer significant mechanical property advantages through the principle of combined action, thereby providing properties that are distinct from their single-material counterparts [1]. Thus, developing multi-material configurations holds potential for a wide range of applications, notably in the aerospace, automotive, construction, and medical industries [2-4]. For bi-materials and composites, failure often occurs at the interface between the two materials—a failure referred to as delamination [5,6]. When acted upon by an external force, cracks typically initiate at or around the interface because of a stress field singularity, resulting in crack growth as a primary failure mechanism [7-9]. Within bi-material systems, there are two bond failures to observe: adhesive and cohesive. Cohesive failure is where the material breaks away/fractures within itself (failure occurs in the bulk of the one material) while adhesive failure is where one material breaks away from the other material (failure occurs at the bi-material interface, delamination) [10]. Additionally, adhesion strength between interfaces correlates to the surface area between the interfaces, so increasing surface area between the interfaces will generally increase its strength [11-13]. Therefore, geometric patterns and designs create stronger adhesion between the interfaces, thus increasing the strength of the bi-material specimen [13].

Moreover, conventional manufacturing approaches involve multiple steps which introduce non-uniform stress distributions, are labor-intensive, and have far worse resolution and accuracy controls with regard to the geometric patterns and designs that can be resolved [9,14,15] while additive manufacturing techniques can bypass such multi-material restrictions. As many additive manufacturing processes and materials are still relatively new, there remains knowledge gaps for mechanical properties and processing parameters that can impede more wide-spread adoption [16]. One form of additive manufacturing that has demonstrated the ability to create complex parts with multiple materials is the 3D printing technique of material

jetting, specifically PolyJet 3D printing, which harness inkjets that allow for multiple photopolymer droplets (and sacrificial support materials) to be dispensed in parallel to build 3D objects *via* line-by-line, layer-by-layer protocols [17-19]. Additionally, this technology allows for the production of parts with high geometric sophistication [17-20].

A previous report examined the application of fractal geometry to design where composite samples, composed of compliant Agilus30 and comparatively rigid VeroMagentaV, showed enhanced mechanical properties and increased load-bearing capacity for interlocking [20]. Using space-filling curve reinforcements (specifically, the Peano curve) in the bulk of the Agilus30, the investigators revealed enhanced stiffness for designs featuring second order Peano and horizontal-oriented reinforcements; however, no design existed at the interfaces between the two materials, and these areas were vulnerable to tensile forces as cracks initiated and propagated at these locations until total failure of the printed samples [20]. Similarly, another study, utilizing PolyJet printing to create specimens with different compositions of VeroMagentaV and Agilus30, displayed that the interface of the bi-materials withstood the stretching forces involved in tensile testing with increasing VeroMagentaV content [21]. Moreover, in a prior report by Hubbard *et al*. in which they harnessed PolyJet 3D printing to create multi-material soft robots, including a swimming robot and a robotic "hand" capable of playing video games, the researchers also examined multi-material PolyJet 3D printing-based fluidic capacitors and found that distinct geometric patterns between the material boundary interface resulted in different burst pressures during fluidic loading [22]. Additional work, investigating the use of multi-material 3D printing on a combustion-powered robot with a rigid plastic core and a soft polymer exterior, revealed that the vast difference in elastic modulus between the multi-materials created a beneficial stiffness gradient that enhanced the desired performance of the robot [23]. Therefore, understanding the properties of such multi-material interfaces is important to emerging applications, yet the majority of previous research on PolyJet-based prints has focused primarily on testing single-material systems [16-18,24]. Given the increasing interest in material jetting and PolyJet 3D printing, in particular, as a pathway to multi-material manufacturing in fields including robotics, fluidic circuitry, and microfluidic technologies [22,23], this study suggests that multi-material interface geometry should be considered appropriately for future applications. Thus, investigations of the relationships connecting multi-material interface geometry to mechanical performance are in critical demand.

2. MATERIALS AND METHODS

2.1. Interface Geometry Calculations

There are numerous ways to potentially pattern the geometry at the bi-material interface, so design criteria were employed to determine the optimal configuration. The criteria chosen to evaluate the designs were moment for uniaxial tension, shape factor (which measures the strength of design based on the amount of material used *versus* its moment), and the surface area between the interfaces as this has been correlated to increased adhesion strength [11-13,25]. The shape of the design geometry and then the corresponding surface area based on the feature size of the chosen shape were used to select the interface designs. The moments (I) of common shapes were calculated using Eqs. 1-5:

$$I_{square}(mm^4) = \frac{b^4}{12} \quad (1)$$

$$I_{triangle}(mm^4) = \frac{a^4}{32\sqrt{3}} \quad (2)$$

$$I_{circle}(mm^4) = \frac{\pi}{4} r^4 \quad (3)$$

$$I_{hollow\ circle}(mm^4) = \pi r^3 t \quad (4)$$

$$I_{hollow\ square}(mm^4) = \frac{2}{3} b^3 t \quad (5)$$

where b refers to the base of the square and hollow square respectively; a refers to the side of the equilateral triangle, r refers to the radius of the circle, and t refers to the thickness of the cross section in the hollow circle and hollow square respectively. These moment calculations were carried out for each shape and at each distinct feature size of the shape. Similarly, the shape factors (*SF*) of hollow circle and hollow square were determined using Eqs. 6-7 while the shape factors of the square, triangle and circle simplified to constant values, 1.00, 1.15, and 0.955 respectively, due to their geometries. Additionally, the design proportions for each common shape remained the same as the feature size increased so that the shape factor remained constant for all design iterations regardless of feature size.

$$SF_{hollow\ circle} = \frac{3}{\pi}\left(\frac{r}{t}\right) \quad (6)$$

$$SF_{hollow\ square} = \frac{1}{2}\left(\frac{b}{t}\right) \quad (7)$$

The hollow square design utilized all space between the interfaces to increase the surface area given the design samples were cuboids with overall dimensions of 30 mm × 90 mm × 10 mm. The control samples, whose interfaces contained no geometric design (flat bi-material interface), had a surface area of 300 mm^2 from the width of 30 mm and thickness of 10 mm. Since the control samples have the two materials lie flush at the interface with no design, these samples serve as a baseline to determine the utility of geometric designs at the interface to increase strength. Conversely, the surface area of the geometric designs was examined using a modified version of the surface area equation for a rectangular prism:

$$SA(mm^2) = 2(b^2 + 2bx) \quad (8)$$

where b is the base of the hollow square and x is depth of feature. The surface area calculations showed that the greatest increase in surface area resulted from the 0.5 mm design, and the remaining surface area calculations predictably decreased with the increasing feature size (Fig. 1). The depth of the hollow

squares was chosen to be 10 mm at each interface for a total of 20 mm through each sample. 10 mm was the maximum distance that did not interfere with the tensile testing setup, thus allowing the largest possible gauge length (40 mm).

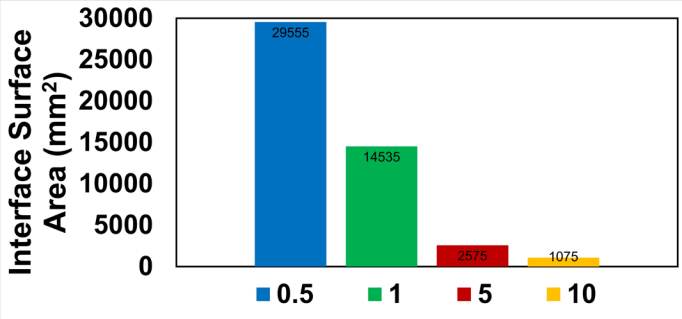

FIGURE 1: CALCULATED SURFACE AREA BETWEEN THE BI-MATERIAL INTERFACES.

2.2. PolyJet 3D Printing Process

The samples were modeled using the CAD software Autodesk Inventor 2023 (Fig. 2A-E) and were then exported as two distinct STL files with each file corresponding to either the compliant or rigid material; the support material was generated automatically by the printer software. The STL files were imported into the computer-aided manufacturing (CAM) software, GradCAD Print (Stratasys), and then manufactured using a Stratasys Objet500 Connex 3 Multi-Material 3D printer. The print time took roughly 16 hrs, with Stratasys proprietary commercial materials of: Agilus30 Black, used for the flexible material, VeroWhite, used for the rigid material (Fig. 2F), and SUP706, used for the water-soluble support material. After printing, the support material was initially removed using water jetting, and then the samples were submerged in a chemical solution bath (97% DI water, 2% NaOH, and 1% Na_2SiO_3) for 4 hrs to remove any remaining support material. Following post-processing, the samples had no visible surface defects or printing errors.

Regarding print parameters, careful consideration was given to the build orientation and support material options. Following previous results, the samples were printed horizontally in the x-direction as it was found that samples printed in the x-direction were characterized by higher tensile strength than samples printed vertically in the z-direction [18], and the samples were isolated to one area on the build plate with each design in an individual row to ensure their mechanical integrity [24,26,27]. The five different interface configurations were each evaluated on four printed specimens (n=4) for a total of 20 printed specimens (Fig. 2G) which resulted in a total build dimension of 90 mm × 190 mm × 55 mm. Moreover, support material for PolyJet printing has two distinct options for surface finish: glossy mode and matte mode. The mode chosen for the support material can impact mechanical integrity as parts generally end up breaking in places where the part goes from glossy to matte, and it has also been suggested that utilizing support material throughout the print creates designs with better geometry and greater dimensional accuracy [17,24,26]. Thus, the specimens were printed in matte mode to ensure uniform surface finish and mechanical integrity.

2.3. Tensile Test Parameters

In order to evaluate the strength at the interface, uniaxial tensile testing was performed on the samples. Testing was initiated using the Tinius Olsen H25K-T benchtop universal testing machine with the Vero sides, directly adjacent to the designed interface sections of the samples, being placed into the friction vice grips. The designed interfaces were not touching and were not placed into the vice grips. To effectively obtain the stress and strain relationship, the uniaxial testing was performed with guidance from ASTM D638 in addition to the work by Subhas et al. [28] and Harding et al. [29], and testing maintained a uniform strain rate of 12.5 mm/min across all samples.

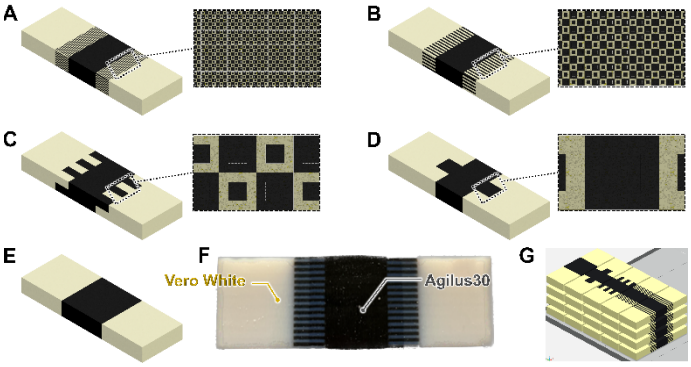

FIGURE 2: CAD RENDERINGS AND INTERNAL CROSS-SECTIONS OF (A) 0.5 MM DESIGN SAMPLE; (B) 1.0 MM DESIGN SAMPLE; (C) 5.0 MM DESIGN SAMPLE; (D) 10.0 MM DESIGN SAMPLE. (E) CAD RENDERING OF PLANAR CONTROL SAMPLE; (F) LABELED POLYJET PRINTED DESIGN SAMPLE; (G) PRINT ORIENTATION OF THE SAMPLES ON OBJET500 CONNEX 3 PRINTER.

2.4. Statistical Analysis Methods

Data obtained from tensile testing was then evaluated using Student's t-test, a statistical hypothesis test, to determine the statistical significance between the control samples and the patterned interface samples. Statistical significance indicated that the observed difference between the samples was convincing enough to demonstrate that the average maximum strain or the average maximum tensile stress between the patterned samples and control differed substantially.

3. RESULTS AND DISCUSSION

Statistical analysis of the tensile testing showed that the patterned interface (non-control) samples were statistically significant when compared to the control samples for strain (Fig. 3A) as the average maximum strain for the control was 101.1% while the average maximum strain for the 0.5 mm, 1 mm, 5 mm, and 10 mm samples were 71.1%, 72.8%, 70.5%, and 68.4% respectively. Conversely, for stress, only the 0.5 mm and 1.0 mm samples showed statistical significance as their average maximum stresses (1.304 MPa and 1.332 MPa, respectively)

differed notably when compared to the control samples (Fig. 3B) which had an average maximum stress of 1.074 MPa. This infers that the 0.5 mm and 1 mm are the only design samples that offer a statistical improvement of strength when compared to the control sample and suggests that the feature size of the hollow square design be in the range of these values (0.5 mm-1 mm).

Given it had the largest increased surface area, the 0.5 mm samples should have theoretically been the strongest sample. However, the 0.5 mm samples also pushed the feature resolution limits of the Objet500 printer which probably resulted in print defects (*e.g.*, voids and small cracks) that hampered mechanical performance. These print defects could be contributed to a variety of factors; perhaps, the different cooling rates and shrinkage rates (*i.e.*, CTE) of the materials, especially in very small areas where the materials overlapped. Moreover, the presence of defects at these smaller features sizes could explain why the 0.5 mm samples had slightly less strength than the 1 mm samples. Consequently, the 1 mm samples recorded the greatest average tensile strength. The design features for these specific samples were within the printer's size/feature resolution of 0.016-0.030 mm which probably resulted in little to no print defects. Surprisingly, the control samples demonstrated greater strength than the 5 mm and 10 mm design samples, which had average maximum stresses of 1.0382 MPa and 1.0514 MPa respectively. Since the 5 mm and 10 mm samples have large features within the feature resolution of the printer, print defects presumably did not largely contribute to the poor performance. Likely, the geometric design is primarily culpable, and it is also feasible that at a certain feature size there is no longer an advantage to having a design at the interface, a point of diminishing returns.

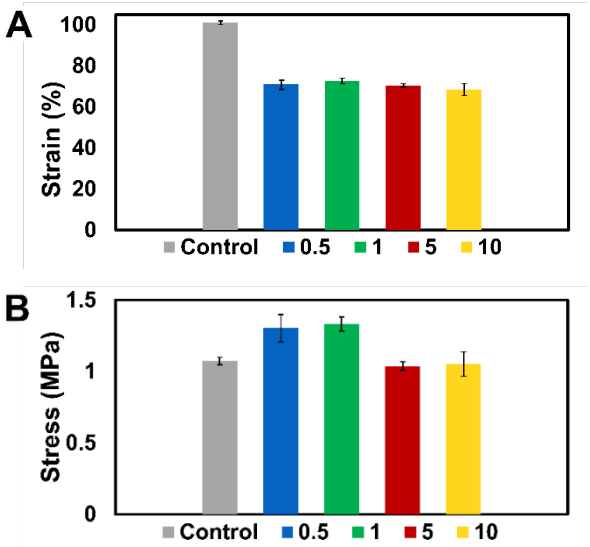

FIGURE 3: (A) COMPARISON OF AVERAGE MAXIMUM STRAIN FOR DESIGN SAMPLES; (B) COMPARISON OF AVERAGE MAXIMUM TENSILE STRESS FOR DESIGN SAMPLES.

Moreover, the fracture behavior and crack propagation during tensile testing provided additional insight into the performance of the samples. All of the samples, besides the 5 mm samples, showed cohesive failure as they did not fail at the interface but rather in the Agilus30 (Fig. 4A-E). Intuitively, this may indicate that the samples are more reflective of the tensile strength and elongation of Agilus30 rather than the Vero material; however, reviewing the fracture behavior of each design sample (Fig. 4A-E) is more indictive of the range of tensile stresses observed.

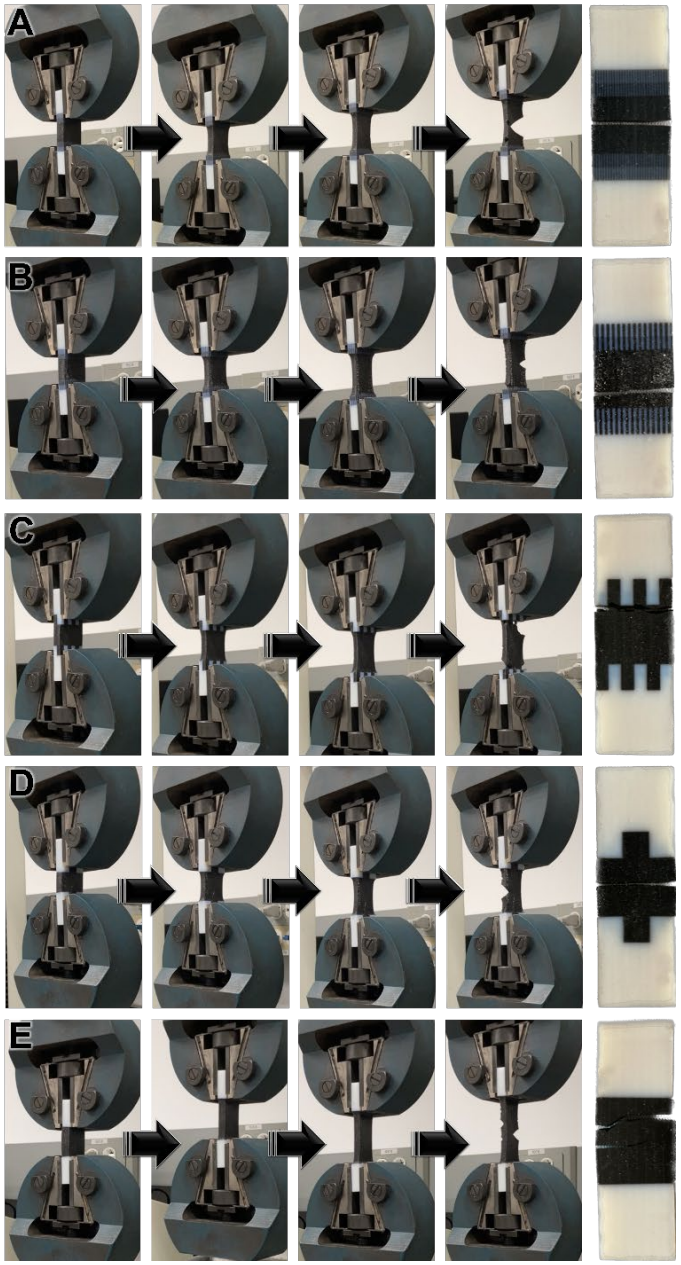

FIGURE 4: FRACTURE PROGRESSION AT 10 SECOND INTERVALS DURING TENSILE TESTING AND CORRESPONDING FRACTURE PATTERN OF (A) 0.5 MM DESIGN SAMPLE; (B) 1.0 MM DESIGN SAMPLE; (C) 5.0 MM DESIGN SAMPLE; (D) 10.0 MM DESIGN SAMPLE; (E) PLANAR CONTROL SAMPLE.

To understand the mechanism that caused the 5 mm samples to exhibit adhesive failure at the interface, the design geometry needs to be reviewed. Recall that the 0.5 mm, 1 mm, and 5 mm samples had asymmetric interface designs with both Vero and Agilus30 at the corners/edges of their designs, whereas the 10 mm samples had a symmetric design with only Vero at the edges. As the feature size increased from the 0.5 mm samples to the 5 mm samples, the amount of crack propagation at the interface also increased until failure occurred at the interface for the 5 mm samples. Examining this fracture behavior reveals that there is a critical feature size which is the maximum size that the base of the hollow square design can be before it leads to failure at the interface. Alternatively, in the context of the fracture behavior, critical feature size can be thought of as allowable flaw size. Since Agilus30 is the weaker of the two materials at the interface, it allowed cracks to form and propagate faster than in Vero. Furthermore, the Agilus30 would initialize cracks and propagate until it reached the Vero section where propagation would slow down. Initially, for the 0.5 mm and 1 mm samples, this did not contribute significantly to either the fracture behavior or the values of tensile strength as the crack lengths were relatively small. These initial cracks at the Agilus30 edges of the interface would propagate slowly or even cease for the 0.5 mm and 1 mm samples at the next Vero layer; this would then lead to crack formation and propagation in the bulk of the Agilus30 until failure occurred. However, when the feature size increased to 5 mm, the crack length increased accordingly such that less stress was required to cause failure at the interface.

Another anomaly amongst the testing data was the 10 mm samples elongating least out of the non-control samples as this opposes the trend that the elongation before failure increases with increasing feature size. However, the amount of VeroWhite in the 10 mm samples and the feature size of these Vero regions were greater than the other samples which probably caused the 10 mm samples to exhibit strain behavior more consistent with the stiffer Vero rather than the flexible Agilus30. These large Vero regions at the edges may have also been counter-intuitive in strengthening the 10 mm samples as there was no deformation at the interface causing cracks to form and propagate in the bulk of the Agilus30. Consequently, stress was concentrated in the Agilus30, leading to premature failure.

Overall, the results of tensile testing with statistical analysis and fracture behavior observations suggest that a hollow square design with a feature size between 0.5 mm and the critical feature size (between 1 mm and 5 mm) will produce samples with the greatest tensile strength. Also, in the context of this study, cohesive failure was more desirable for the samples than adhesive failure as it demonstrated that the interface bond between the Vero and Agilus30 was stronger than the internal structure of the Agilus30.

4. CONCLUSION

Understanding the impact of interface geometry on the strength of bi-material designs is crucial in advancing the use of multi-material PolyJet printing for applications where single-phase materials cannot meet demands. Here five geometrically different bi-material designs were presented and tested by performing uniaxial tensile tests under uniform strain rates. Contrary to expectations, increasing the surface contact between the two distinct materials by changes in geometric design did not necessarily increase its strength. It was also determined that there was a certain range of feature sizes (critical feature size) for the hollow square samples where the strength and fracture behavior both deviated. Future research into utilizing fractal geometry in the bulk of the weaker material (Agilus30) and/or at the bi-material interface shows promise and could build upon the work laid out in this paper. Furthermore, more application-specific geometries could now be investigated to fit target needs and various environmental conditions (*e.g.*, temperature, humidity, pH). In addition, as researchers have demonstrated alternative types of multi-material 3D printing approaches, such as “Direct Laser Writing” [30,31], it is possible these results could be applied beyond PolyJet 3D printing specifically.

ACKNOWLEDGEMENTS

The authors would like to thank R.J. Bonenberger for helpful discussions and assisting with testing set-up. Tensile testing was performed at the George E. Dieter, Jr. Materials Instructional Lab (GEDMIL). This work was supported in part by U.S. National Science Foundation Award Number 1943356.

REFERENCES

[1] Callister, W.D., and Rethwisch, D.G., 2012, *Fundamentals of Materials Science and Engineering: An Integrated Approach, fourth ed.*, John Wiley and Sons, NY.

[2] Sochol, R.D., Sweet, E., Glick, C.C., Venkatesh, S., Avetisyan, A., Ekman, K.F., Raulinaitis, A., et al., 2016, “3D Printed Microfluidic Circuitry via MultiJet-based Additive Manufacturing,” *Lab Chip*, 4, pp. 668-678.

[3] Hayes, B., Hainsworth, T., and MacCurdy, R., 2022, “Liquid–Solid Co-Printing of Multi-Material 3D Fluidic Devices via Material Jetting,” *Addit. Manuf.*, 55(102785).

[4] MacCurdy, R., Katzschmann, R., Kim, Y., and Rus, D., 2016, “Printable Hydraulics: A Method for Fabricating Robots by 3D Co-printing Solids and Liquids,” 2016 IEEE International Conference on Robotics and Automation (ICRA), Stockholm, Sweden, May 16-21, 2016, pp. 3878-3885.

[5] Nakamura, T., Okumura, M., and Hasebe, N., 1992, “Cracking and Debonding on Bimaterial Interface under Uniform Loading,” *J. Eng. Mech.*, 118(6), pp. 1113-1128.

[6] Sehr, S., Amidi, S., and Begley, M.R., 2019, “Interface Delamination vs. Bulk Cracking along Wavy Interfaces,” *Eng. Fract. Mech.*, 206, pp. 64-74.

[7] Djoković, J.M., Nikolić, R.R., Bujnak, J., Hadzima, B., and Tomić, R., 2020, “Some Aspects of the Three-dimensional Interface Cracks Analysis,” *Teh. Vjsen.*, 27, pp. 1-4.

[8] Kinloch, A.J., Thrusabanjong, E., and Williams, J.G., 1991, “Fracture at Bimaterial Interfaces: The Role of Residual Stresses,” *J. Mater. Sci.*, 26, pp. 6260–6270.

[9] Luo, X.F., and Aoki, S., 1992, “Crack Growth on Elasti-c-plastic Bimaterial Interfaces,” *Int. J. Fract.*, 57, pp. 365-379.

[10] Singh, Y., Kumar, J., Singh, I., and Rakesh P.K., 2022, "Joining Behavior of Natural Fiber Reinforced Polymer Composites," Joining Processes for Dissimilar and Advanced Materials. Woodhead Publishing, Cambridge, UK, pp. 33-63.

[11] Varias, A.G., O'Dowd, N.P., Asaro, R.J., and Shih, C.F., 1990, "Failure of Bimaterial Interfaces," *Mater. Sci. Eng. A*, 126(1-2), pp. 65-93.

[12] Evans, A.G., Rühle, M., Dalgleish, B.J., and Charalambides, P.G., 1990, "The Fracture Energy of Bimaterial Interfaces," *Mater. Sci. Eng. A*, 126(1-2), pp. 53-64.

[13] Boresi, A.P., and Schmidt, R.J., 2003, *Advanced Mechanics of Materials, sixth ed.*, John Wiley and Sons, NY.

[14] Needleman, A., and Rosakis, A.J., 1999, "The Effect of Bond Strength and Loading Rate on the Conditions Governing the Attainment of Intersonic Crack Growth along Interfaces," *J. Mech. Phys. Solids*, 47(12), pp. 2411-2449.

[15] Barroso, A., Lauke, B., Mantič, V., and París, F., 2016, "Tensile and Shear Strength of Bimaterial Interfaces within Composite Materials," *Compos. Sci. Technol.*, 124, pp. 81-88.

[16] Gay, P., Blanco, D., Pelayo, F., Noriega, A., and Fernández, P., 2015, "Analysis of Factors Influencing the Mechanical Properties of Flat PolyJet Manufactured Parts," *Procedia Eng.*, 132, pp. 70-77.

[17] Silva, M.R., Pereira, A.M., Sampaio, A.M., and Pontes, A.J., 2021, "Assessment of the Dimensional and Geometric Precision of Micro-Details Produced by Material Jetting," *Materials*, 14(8).

[18] Majca-Nowak, N., and Pyrzanowski, P., 2023, "The Analysis of Mechanical Properties and Geometric Accuracy in Specimens Printed in Material Jetting Technology," *Materials*, 16(8).

[19] Udroiu, R., and Braga, I.C., 2020, "System Performance and Process Capability in Additive Manufacturing: Quality Control for Polymer Jetting," *Polymers*, 12(6).

[20] Wu, C., Do, T.T., and Tran, P., 2021, "Mechanical Properties of PolyJet 3D-Printed Composites Inspired by Space-Filling Peano Curves," *Polymers*, 13(20).

[21] Tee, Y.L., Peng, C., Pille, P., Leary, M., and Tran, P., 2020, "PolyJet 3D Printing of Composite Materials: Experimental and Modelling Approach," *JOM*, 72, pp. 1105-1117.

[22] Hubbard, J.D., Acevedo, R., Edwards, K.M., Alsharhan, A.T., Wen, Z., Landry, J., Wang, K., Schaffer, S., and Sochol, R.D., 2021, "Fully 3D-Printed Soft Robots with Integrated Fluidic Circuitry," *Sci. Adv.*, 7(29).

[23] Bartlett, N.W., Tolley, M.T., Overvelde, J.T., Weaver, J.C., Mosadegh, B., Bertoldi, K., Whitesides, G.M., and Wood, R.J., 2015, "A 3D-printed, functionally graded soft robot powered by combustion," *Science*, 349(6244), pp. 161-165.

[24] Yap, Y.L., Wang, C., Sing, S., Dikshit, V., Yeong, W.Y., and Wei, J., 2017, "Material Jetting Additive Manufacturing: An Experimental Study using Designed Metrological Benchmarks, *Precis. Eng.*, 50, pp. 275-285.

[25] Ashby, M.F., 2011, *Materials Selection in Mechanical Design, fourth ed.*, Butterworth-Heinemann, Oxford.

[26] Mendricky, R., and Soni, R.D., 2022, "Geometric Stability of Parts Produced by 3D Printing," *Teh. Vjsen.*, 29(1).

[27] Stratasys, 2019, "Objet350 and Objet500 Connex 3."

[28] Subhash, G., and Ridgeway, S., 2018, *Mechanics of Materials Laboratory Course*, Morgan & Claypool, CA.

[29] Harding, J., Wood, E.O., and Campbell, J.D., 1960, "Tensile Testing of Materials at Impact Rates of Strain," *J. Mech. Eng. Sci.*, 2(2), pp. 88–96.

[30] Lamont, A.C., Restaino, M.A., Kima, M.J., and Sochol, R.D., 2019, "A Facile Multi-material Direct Laser Writing Strategy," *Lab Chip*, 19, pp. 2340-2345.

[31] Mayer, F., Richter, S., Westhauser, J., Blasco, E., Barner-Kowollik, C., and Wegener, M., 2019, "Multimaterial 3D Laser Microprinting using an Integrated Microfluidic System," *Sci. Adv.*, 5(2).